

Empirical dependence of acoustic transmission scintillation statistics on bandwidth, frequency, and range in New Jersey continental shelf

Mark Andrews

Department of Electrical and Computer Engineering, Northeastern University, 360 Huntington Avenue, Boston, Massachusetts 02115

Tianrun Chen

Department of Mechanical Engineering, Massachusetts Institute of Technology, 77 Massachusetts Avenue, Cambridge, Massachusetts 02139

Purnima Ratilal

Department of Electrical and Computer Engineering, Northeastern University, 360 Huntington Avenue, Boston, Massachusetts 02115

(Received 11 March 2008; revised 1 November 2008; accepted 6 November 2008)

The scintillation statistics of broadband acoustic transmissions are determined as a function of signal bandwidth B , center frequency f_c , and range with experimental data in the New Jersey continental shelf. The received signal intensity is shown to follow the Gamma distribution implying that the central limit theorem has led to a fully saturated field from independent multimodal propagation contributions. The Gamma distribution depends on the mean intensity and the number of independent statistical fluctuations or coherent cells μ of the received signal. The latter is calculated for the matched filter, the Parseval sum, and the bandpassed center frequency, all of which are standard ocean acoustic receivers. The number of fluctuations μ of the received signal is found to be an order of magnitude smaller than the time-bandwidth product TB of the transmitted signal, and to increase monotonically with relative bandwidth B/f_c . A computationally efficient numerical approach is developed to predict the mean intensity and the corresponding broadband transmission loss of a fluctuating, range-dependent ocean waveguide by range and depth averaging the output of a time-harmonic stochastic propagation model. This model enables efficient and accurate estimation of transmission loss over wide areas, which has become essential in wide-area sonar imaging applications. © 2009 Acoustical Society of America. [DOI: 10.1121/1.3037228]

PACS number(s): 43.30.Re, 43.30.Pc, 43.60.Cg [RCG]

Pages: 111–124

I. INTRODUCTION

Acoustic signals transmitted through an ocean waveguide typically scintillate in both time and space upon reception due to multimodal propagation and random variations of the medium and its boundaries. Quantitative knowledge of these received signal fluctuations is often essential in the design of ocean acoustic experiments and in the analysis of subsequent measurements.^{1–3} Extensive research have been conducted to investigate the effects of random oceanographic variations on the acoustic field propagated through continental shelf^{4–9} as well as in the deep ocean waveguides.^{10,11} The corresponding statistical analyses, however, have typically been limited to either narrowband or broadband transmissions with a fixed time-bandwidth product TB and not as a function of transmitted signal's bandwidth, frequency, and time duration.

Here we determine the scintillation statistics of acoustic transmissions as a function of transmitted bandwidth B , center frequency f_c , and range in a continental shelf waveguide for signals where the transmitted time-bandwidth product TB may be large. Signals with large TB are important for obtaining high range resolution and high signal-to-noise ratio in many ocean-acoustic applications by use of matched filter

(MF)^{12,13} receivers. We use data obtained from the Main Acoustic Experiment (MAE) 2003 (Refs. 2 and 14) of the Office of Naval Research Geoclutter Program conducted at the Strataform site on the New Jersey continental shelf. Broadband pulses of varying bandwidths and time-bandwidth products in the low to midfrequency range transmitted by a vertical source array and measured on a towed horizontal receiving array are analyzed.

We show that received signal intensity follows the Gamma distribution.^{15,16} This implies that the central limit theorem has led to fully saturated fluctuations at the receiver which arise from independent multimodal propagation contributions. The Gamma distribution depends on the mean intensity and the number of independent statistical fluctuations or coherence cells μ of the received signal. We determine the number of coherence cells empirically by Rice's method¹⁷ for several standard receivers commonly used in ocean acoustics, such as the MF, the Parseval sum (PS), and the bandpassed center frequency. We show that the number of independent statistical fluctuations of the received signal μ is not equal to the time-bandwidth product TB of the original transmitted signal for large TB but is typically an order of magnitude smaller. This implies that much of a large TB

signals' original bandwidth remains statistically correlated after propagation through the random waveguide. We then show that the number of received fluctuations μ increases monotonically with the relative bandwidth B/f_c of the transmitted signal.

Our analysis provides a useful method for determining the scintillation statistics of signals transmitted with arbitrary bandwidth in the low to midfrequency range through a fluctuating continental shelf waveguide. This knowledge can then be applied to aid in the design of ocean acoustic experiments and in subsequent measurement analysis. It can also be used to determine error bounds on parameter estimates and determine sample sizes necessary to reduce estimation errors so that they fall within tolerable ranges.^{13,18}

In active sonar applications, the MF is extensively applied to maximize signal-to-noise ratio in target detection and enhance range resolution in target localization.^{2,12,19–21} The *peak* MF output is often used to determine both the scattered field level and the location of a discrete target.^{22–25} Matched filtering is a coherent process where the received signal is correlated to the transmitted waveform. Since acoustic signals propagated long ranges through an ocean waveguide are distorted from multipath propagation and modal dispersion, the MF output becomes highly susceptible to mismatch in an ocean waveguide.

Contrary to the situation in free space where the MF output does not vary with source-receiver range, we show that in an ocean waveguide it degrades significantly and with increasing range due to the effects of cumulative modal dispersion. We show that this degradation must be taken into account to reliably infer source level, scattering strength, or target strength from active sonar data in a continental shelf waveguide, and provide an approach to do so. In free space environments, the fact that the peak output of the MF equals^{26,27} the PS energy is often used to normalize the MF output. We show that another approach must be used in an ocean waveguide because the peak MF output tends to have a lower mean and higher standard deviation than an incoherent Parseval energy summation of the received signal.

When a wide-area sonar system is used to study scattering from distributed scatterers, such as a large fish shoal or the sea bottom, over areas spanning tens of thousands of km² with varying bathymetry, it is necessary to correct for transmission loss (TL) over these vast areas.^{2,14,28–31} Since the waveguides are often random and the transmitted signals are often broadband, the number of computations required per radial with a range-dependent waveguide propagation model such as the parabolic equation make brute-force Monte Carlo simulations impractical for many applications that require rapid analysis of hundreds of wide-area sonar images typically collected in a single day at sea.^{2,14}

Here, we provide an approach for rapidly and accurately estimating broadband TL expected over wide areas. The approach uses the range-dependent acoustic model (RAM)³² to calculate the acoustic intensity at the center frequency of the signal, after propagation through a waveguide randomized by sound speed fluctuations. A combination of range and depth averaging is then used to approximate the *expected* broadband intensity in a fluctuating environment. For the

New Jersey continental shelf, we show that only three to five Monte Carlo simulations are required to converge on the mean TL for each radial. This approach has proven to be crucial in enabling rapid wide area scattering strength analysis in recent ocean imaging experiments.^{2,14}

We describe relevant aspects of the MAE 2003 field experiment in Sec. II and present statistical analysis of the acquired data. In Sec. III, we describe our method for rapidly estimating the TL expected over wide areas and show how the method can be calibrated using the broadband data collected from the MAE 2003 field experiment.

II. BROADBAND TRANSMISSION DATA

A. Data collection

The experiment was conducted from April 27 to May 15, 2003 (Ref. 2 and 14) on the New Jersey Strataform.³³ A moored vertical source array centered at a depth of 47 m transmitted Tukey-shaded linear frequency modulated (LFM) pulses in three distinct frequency bands, 390–440 Hz, 875–975 Hz, and 1250–1400 Hz, each 1 s in duration. The source array consists of seven XF-4 transducer elements spaced 1.63 m apart for the lower band, and ten mod-30 elements spaced 0.8 m apart for the two higher bands. The signals are radiated azimuthally symmetric about the source array. The signals were received on a horizontal hydrophone array of which one hydrophone was desensitized with a lower gain setting, giving it a larger dynamic range for recording the one way propagated waveforms. The receiving array was towed at depths between 30 and 50 m with a speed of 2 m/s along track lines 10 km long for 30 different tracks during the days of May 5–15. On four of these tracks, the two higher bandwidths were simultaneously transmitted, while in the remaining 26 tracks, the lower frequency band was transmitted. The source transmitted pulses at every 50 s interval in which time the receiver array moved approximately 100 m.

The three distinct source locations and tracks of the receiver array for the data analyzed are overlain on the bathymetry at the experiment site shown in Fig. 1. The bathymetric variations are fairly benign, with depths ranging from 65 to 80 m. The seafloor geoaoustic parameters on the New Jersey Strataform are well characterized.³⁴ The seafloor is mostly sand with a mean density, sound speed, and attenuation of approximately 1.9 g/cm³, 1700 m/s, and 0.8 dB/ λ , respectively, in the region where the data were collected.³⁴ Internal waves randomize the sound speed profiles over time and space in the continental shelf region. During the experiment, over 100 sound speed profiles were measured at the experiment site, as shown in Fig. 2.

The effect of propagation through the random and dispersive multimodal ocean waveguide is illustrated in Fig. 3 for two typical transmissions received at ranges of 2.5 and 13 km. The signal is reduced in amplitude due to cylindrical spreading loss and attenuation in the sea bottom. The signal envelope, MF signal, and spectral shape are also substantially modified. The MF signal illustrates the dispersion of

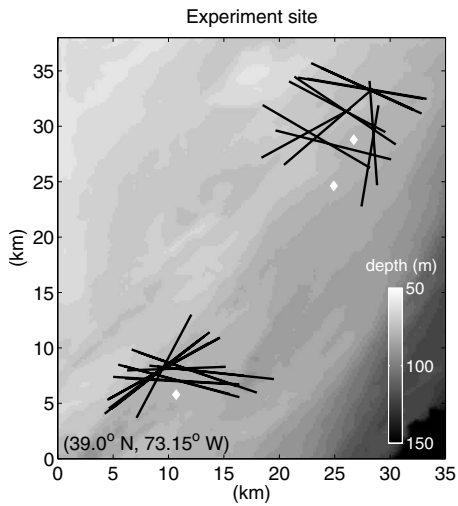


FIG. 1. The locations of the source (white diamond) and receiver tracks (black lines) are shown overlain onto the bathymetry on the New Jersey Strataform. The bathymetry data have 30 m resolution and are obtained from high-resolution bathymetric surveys described in Ref. 33. Coordinates of the southwest corner of the image are 39.0° N, 73.15° W.

the multipath arrivals; there is one large initial peak formed by low-order modes as well as smaller peaks later in time from higher-order modes.

B. Data processing

Let $\Psi(\mathbf{r}|\mathbf{r}_o, t)$ be the received pressure in time t at receiver location \mathbf{r} from a source at \mathbf{r}_o with complex spectral amplitude $\Phi(\mathbf{r}|\mathbf{r}_o, f)$ for frequency f obtained by Fourier transform analysis,

$$\Phi(\mathbf{r}|\mathbf{r}_o, f) = \int_T \Psi(\mathbf{r}|\mathbf{r}_o, t) \exp(-j2\pi ft) dt, \quad (1)$$

where T is the time window used to isolate the direct arrival³⁵ from reverberation and other noise sources. T is chosen to be 2 s, including 0.5 s before the initial arrival of the signal and 0.5 s after the 1 s duration signal to sufficiently capture the signal and dispersion of the late arrivals.

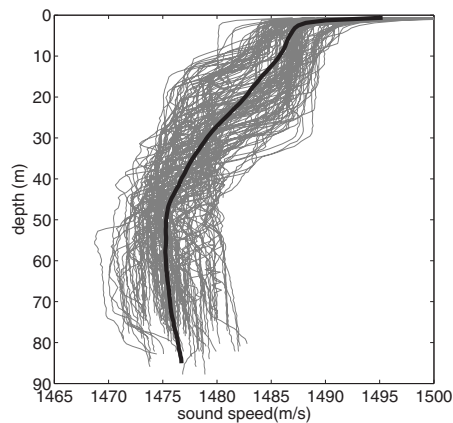


FIG. 2. Over 100 sound speed profiles were experimentally collected during the Main Acoustic Clutter Experiment (2003) on the New Jersey continental shelf by deploying both conductivity-temperature-depth sensors and expendable bathythermographs.

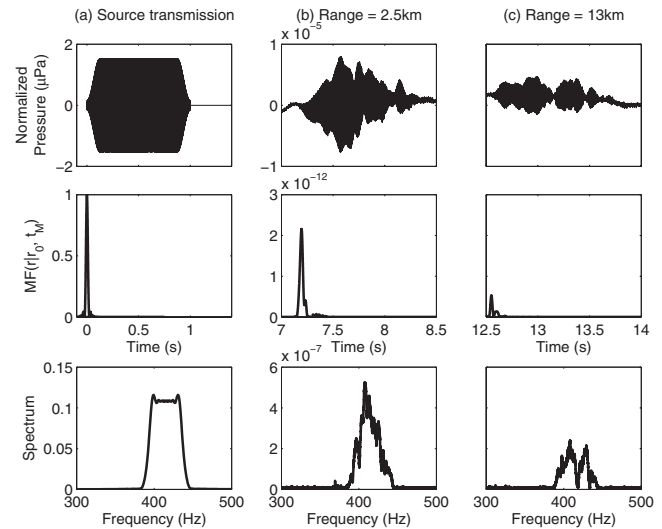


FIG. 3. (a) The transmitted signals Tukey-shaped LFM waveform is compared to the received signal at (b) ranges of 2.5 km and (c) 13 km. The signal envelope (top), the MF signal (middle), and signal spectrum (bottom) are plotted for comparison.

Integrating the magnitude squared spectrum over the signal bandwidth $B=f_f-f_i$, we obtain

$$E_{PS}(\mathbf{r}|\mathbf{r}_o) = \int_{f_i}^{f_f} |\Phi(\mathbf{r}|\mathbf{r}_o, f)|^2 df. \quad (2)$$

By Parseval's theorem $E_{PS}(\mathbf{r}|\mathbf{r}_o)$ is proportional to the signal energy. Scattered reverberation and noise integrated into the PS occurring within the time window and frequency band is considered to be negligible in comparison to the direct signal from the source. Figure 4 shows the PS energy for all transmissions in a single track as a function of integration time starting 1 s prior to the pulse arrival. Here we see that increasing the time window beyond the signal duration to in-

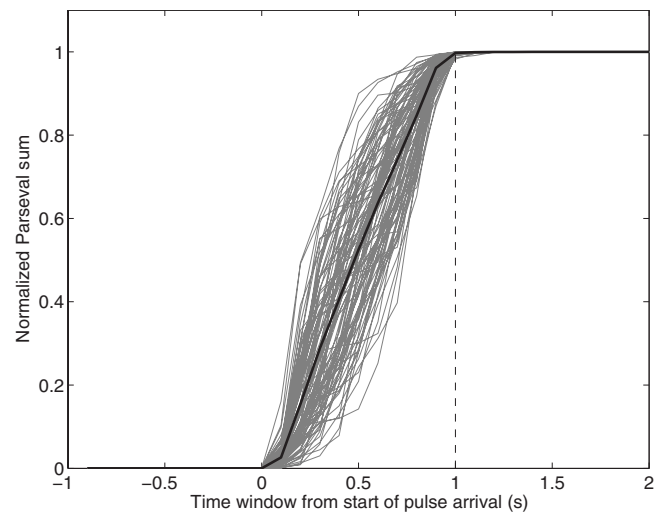


FIG. 4. The normalized PS for all transmissions in a track are illustrated as a function of the integration time window. The time window is measured from 1 s prior to the pulse arrival and increased it to include the 1 s duration signal as well as 1 s afterward to measure the effects of late multipath arrivals, noise, and reverberation on the PS value. Here we see that the entire PS energy is well contained within the 1 s signal duration and therefore has negligible contributions from reverberation and noise.

clude reverberation and noise has negligible effect.

For sonar applications, our primary interest is the MF energy, where the filter is a replica of the original transmitted signal $q(t)$. The normalized MF is given by^{19,26} $h(t|t_M) = Kq(t_M - t)$, and its Fourier transform is $H(f|t_M) = KQ^*(f)\exp(-j2\pi ft_M)$, where t_M is the delay time of the MF, $Q(f)$ is the Fourier transform of the source signal, and $K = (\int_{f_i}^{f_f} |Q(f)|^2 df)^{-1/2}$ is the normalizing factor. The MF output is then

$$\begin{aligned} \text{MF}(\mathbf{r}|\mathbf{r}_o, t_M) &= |h(t|t_M) * \Psi(\mathbf{r}|\mathbf{r}_o, t)|^2 \\ &= \left| \int_{f_i}^{f_f} \Phi(\mathbf{r}|\mathbf{r}_o, f) H(f|t_M) \exp(j2\pi ft) df \right|^2 \\ &= \left| \int_{f_i}^{f_f} \Phi(\mathbf{r}|\mathbf{r}_o, f) KQ^*(f) \exp(j2\pi f(t - t_M)) df \right|^2. \end{aligned} \quad (3)$$

As was shown in Fig. 3, the MF output has one strong peak due to the direct arrival of the signal. Later multipath arrivals may be present if they can be resolved from the primary peak. To obtain the MF energy contained in the primary arrival, we take the maximum value of Eq. (3),

$$E_{\text{MF}}(\mathbf{r}|\mathbf{r}_o) = \text{MF}(\mathbf{r}|\mathbf{r}_o, t_M)|_{\text{max}}. \quad (4)$$

In unbounded free-space media, this maximum occurs when $t_M = |\mathbf{r} - \mathbf{r}_o|/c$, where c is the sound speed, but in a dispersive waveguide there may be some time delay. For discrete targets, the scattered signal's peak MF output is dominant and often the only peak that stands above background reverberation and ambient noise.

For a LFM signal, the intensity at a single frequency, for instance, the center frequency f_c , can be approximated as an *instantaneous intensity* when the LFM signal sweeps through the signal bandwidth over the signal duration. The pressure magnitude squared spectrum bandlimited to 1 Hz at the center frequency, $|\Phi(\mathbf{r}|\mathbf{r}_o, f_c)|^2$, multiplied by the signal bandwidth,

$$E_{\text{CF}}(\mathbf{r}|\mathbf{r}_o, f_c) = |\Phi(\mathbf{r}|\mathbf{r}_o, f_c)|^2 B, \quad (5)$$

then has the same units as the PS and MF energies and can be used for direct statistical comparison.

Taking $10 \log_{10}$ of Eqs. (2), (4), and (5) gives the PS, MF, and CF energy levels in decibel units and we denote these by L_{PS} , L_{MF} , and L_{CF} , respectively. The MF degradation is defined here as

$$D_{\text{MF}}(\mathbf{r}|\mathbf{r}_o) = L_{\text{PS}}(\mathbf{r}|\mathbf{r}_o) - L_{\text{MF}}(\mathbf{r}|\mathbf{r}_o). \quad (6)$$

C. Normal mode modeling of matched filtered signal

Here, we show that a significant portion of the signal's MF energy is contained within the initial direct arrival peak. A normal mode propagation model³⁶ is used to predict modal arrivals of the broadband transmissions. The model determines the acoustic field $\Phi(\mathbf{r}|\mathbf{r}_o, f)$ for a range-independent shallow water waveguide 80 m deep for all frequencies over the signal bandwidth by coherently combining the contribu-

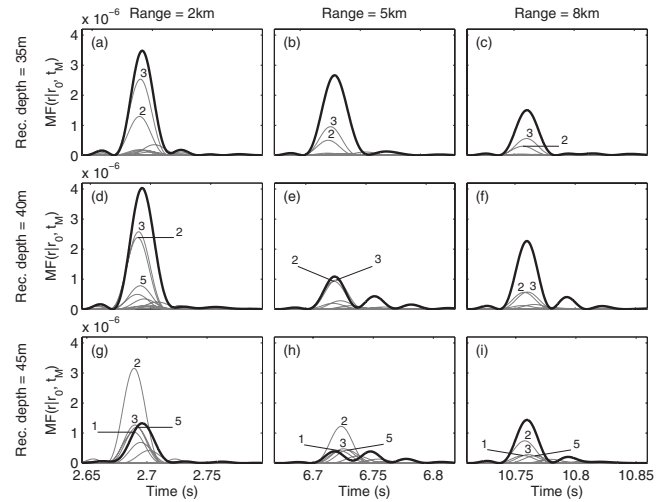


FIG. 5. The Kraken normal mode model is used to simulate the MF signal and compare modal contributions for a receiver at ranges of 2, 5, and 8 km, and depths of 35, 40, and 45 m. The magnitude squared MF output for each mode is shown in gray with the most prominent modes labeled. The modes can combine either constructively or destructively to produce the total matched filtered intensity (black).

tions from the individual source elements centered at 42 m depth. Applying Eq. (3) provides the modeled MF intensity. Seafloor geoacoustic parameters described in Sec. II A and the mean sound speed profile illustrated in Fig. 2 are used to simulate the New Jersey shelf environment.

Figure 5 illustrates the modeled MF signal for receiver ranges of 2, 5, and 8 km and receiver depths of 35, 40, and 45 m, which were typical during the experiment. The modal contributions for the first ten modes in the ocean waveguide are shown in gray with the dominant mode numbers labeled. In each case, the first four modes are unresolved by the primary signal peak, interfering either constructively or destructively to result in the MF intensity, shown in black. Later modal arrivals generally produce small secondary peaks in the MF signal.

While the normal mode model does not incorporate the effects of range-dependent bathymetry and fluctuating sound speed profiles caused by internal waves, it is still useful in determining which modes are dominant, as well as their relative arrival times. Fluctuations from internal waves may increase the modal dispersion effects, and mode coupling may spread the temporal arrivals from particular modes slightly.^{4,7} However, we see that the modal dispersion modeled here is consistent with that seen in the MF data of Fig. 3. For data collected on a single hydrophone, it is impossible to resolve individual modal contributions as is modeled here. At the ranges of interest, we can see that the signal energy is mostly contained within the initial peak.

D. Mean, standard deviation, and number of independent statistical fluctuations

The levels L_{PS} , L_{MF} , and L_{CF} are calculated for each received signal from all 30 tracks. The signal path and corresponding bathymetry from source to receiver for each measurement vary depending on source location, track, and receiver position on the track. The figures will illustrate the

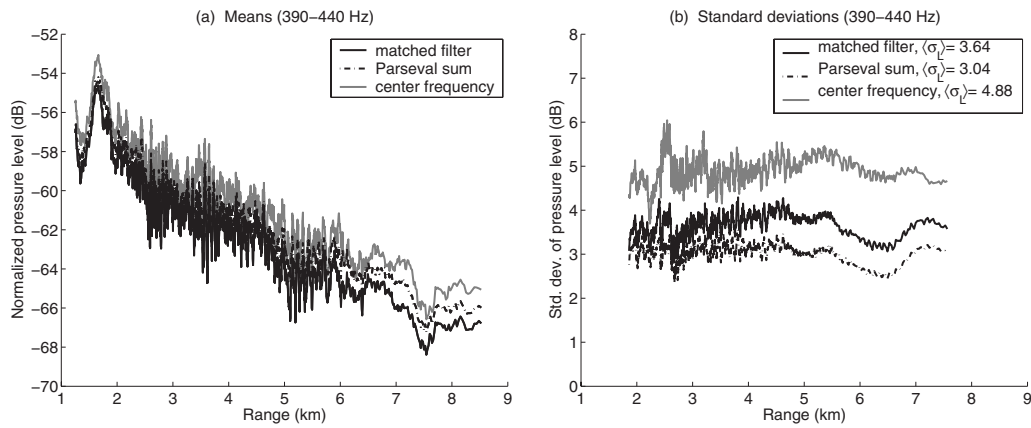


FIG. 6. The one-way propagated broadband transmissions at 390–440 Hz are processed and normalized for a 0 dB re 1 μ Pa at 1 m source level. The (a) means and (b) standard deviations are calculated using a 2 km running window in range for the MF, PS, and the bandpass center frequency energies.

statistics of the lowest band as it is the most plentiful dataset. Results from the higher bands are tabulated. The means and standard deviations for the various measurements taken over a running window of 20 pings along each track are illustrated in Fig. 6 for the 390–440 Hz band. The observed fluctuations in the data are due to both temporal and spatial variations in the medium. The source level fluctuations are small compared to those caused by the environment. The time interval for each 20-ping sequence is 16 min and change in receiver location is 2 km. This distance is greater than the spatial coherence length of approximately 500 m for internal waves in shallow water.^{4,37} The 20-ping averaging is therefore large enough to sample our data over independent fluctuations of the environment caused by internal waves, while still providing a small enough window to observe trends in the means and standard deviations over range. The means and standard deviations from each track are then averaged together. The means are calculated from antilog data and then converted to decibel levels for plotting. This is to avoid potential bias in the mean of log-transformed quantities.¹⁵ The standard deviations are calculated directly from the log-transformed data since they are expected to have uniform standard deviations.¹⁵

The means plotted in Fig. 6(a) illustrate the general intensity decay with range due to spreading, absorption, and scattering losses in the waveguide. Modal interference effects are significant for source-receiver separations less than 2 km. The standard deviations in Fig. 6(b) are largest for L_{CF} and smallest for L_{PS} . The PS measurement integrates over statistically independent fluctuations within the signal duration and bandwidth which reduces its standard deviation. The

MF also utilizes the entire signal duration and bandwidth, but has a slightly higher standard deviation than the PS because the MF degradation is not constant and introduces its own fluctuation.

Using coherence theory, the energy level standard deviation σ_L is related to the number of independent statistical fluctuations or coherence cells μ (Refs. 15 and 16) of the received signal,

$$\sigma_L = (10 \log_{10} e) \sqrt{\sum_{k=0}^{\infty} \frac{1}{(\mu + k)^2}}. \quad (7)$$

Using the experimentally determined standard deviations as an input to Eq. (7), the corresponding μ for the levels L_{CF} , L_{PS} , and L_{MF} are calculated and summarized in Table I for all three bands. The level L_{CF} has a standard deviation close to 5 dB for each band, which corresponds to $\mu \approx 1.2$. The PS for the 50 Hz bandwidth signal from 390 to 440 Hz, for instance, integrates over approximately $\mu = 2.5$ independent statistical fluctuations over the signal duration and spectrum. This is an order of magnitude smaller than the deterministic transmitted signal's own time-bandwidth product of $TB = 50$ for $T = 1$ s and $B = 50$ Hz. This implies that the signal is remaining largely correlated across the bandwidth after propagation through the random waveguide.

The number of independent statistical fluctuations μ of the received signal depends on the relative bandwidth B/f_c of the transmitted signal for signals with a fixed time duration, smaller than its statistical decorrelation time scale. The standard deviation and μ are plotted as a function of relative bandwidth in Figs. 7(a) and 7(b) for the PS energy. We ob-

TABLE I. Standard deviations σ_L of the measurements for each bandwidth are obtained from data analysis described in Sec. II D. The number of independent statistical fluctuations μ are calculated from Eq. (7).

	390–440 Hz		875–975 Hz		1250–1400 Hz	
	σ_L (dB)	μ	σ_L (dB)	μ	σ_L (dB)	μ
Center frequency	4.98	1.16	4.92	1.18	4.98	1.16
Parseval sum	2.99	2.54	3.62	1.86	3.57	1.91
Matched filter	3.64	1.85	4.35	1.41	4.19	1.49
Relative bandwidth B/f_c	0.121		0.108		0.113	

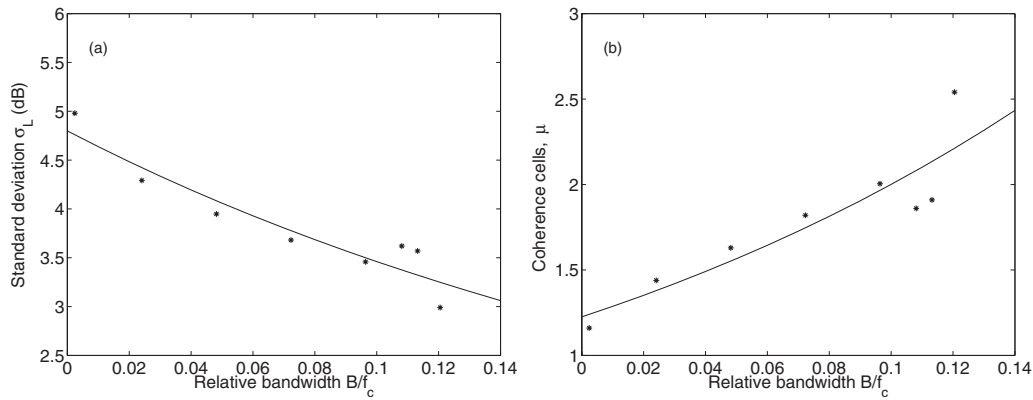


FIG. 7. The PS energy level (a) standard deviations σ_L , and (b) number of coherence cells μ are plotted as a function of relative bandwidth from each of the three bands. The results at other B/f_c ratios are obtained by bandpassing the 390–440 Hz data and performing similar statistical analysis. The equation describing the monotonic fit for (b) is $\mu = A \exp(kB/f_c)$, where parameters $A = 1.23$ and $k = 4.9$. The curve shown in (a) can be obtained from (b) with Eq. (7).

serve the energy standard deviation decreases monotonically with the relative bandwidth, while μ increases monotonically.

The rate of increase in μ with relative bandwidth obtained here from experimental data is much smaller than that obtained in Ref. 8 based on theoretical modeling. There, the number of coherence cells was found to increase from 1 to 20 as the signal bandwidth increased from 0 to 200 Hz for a 1 kHz signal propagating in a waveguide with 100 m water depth at 15 km range. Figure 7(b) shows that this is physically not achievable unless the statistical decorrelation time of the signal is much shorter than the signal duration in that environment. Extrapolating the results in Fig. 7(b), we would obtain only about three coherence cells for a signal with $B/f_c = 0.2$ when its duration is roughly 1 s on the New Jersey shelf, where the acoustic field decorrelation time scale in this waveguide is about 5 min.^{38,39}

When a waveguide is randomized, the multimodal interference pattern is randomized in both space and time. Figure 7(a) suggests that even though the modes are randomized, the intensity fluctuation for the broadband signal are roughly bounded by the peak and trough of intensity variation with range and depth in a nonrandom waveguide. This is expected to be the case when the fluctuations are caused by linear internal waves. When nonlinear internal waves or solitons are present, then much larger standard deviations may be obtained.

The relationship derived in Fig. 7(a) between the standard deviation and relative bandwidth can now be used in experimental design to aid in selecting the appropriate frequency bandwidth for the acoustic transmissions in order to achieve the desired standard deviation in the received signal energy.

E. Statistical distributions

Histograms for the 390–440 Hz bandpassed center frequency data E_{CF} , the broadband PS E_{PS} , and MF energies E_{MF} are shown in Figs. 8–10. The histograms illustrate the distribution of measurements separated in range increments of 500 m. The center frequency data follow the exponential distribution, which has nonzero probability density for $E = 0$, as shown in Fig. 8. This implies that the complex spectral

amplitude $\Phi(\mathbf{r}|\mathbf{r}_o, f_c)$ can be treated as a circular complex Gaussian random variable.¹⁶ This allows us to approximate the E_{CF} measurements as being fully randomized.

The broadband data follow the Gamma distribution¹⁵ parametrized by the number of coherence cells,

$$P(E(r)) = \frac{(\mu/\overline{E(r)})^\mu E(r)^{\mu-1} \exp(-\mu E(r)/\overline{E(r)})}{\Gamma(\mu)}, \quad (8)$$

where $\Gamma(\mu)$ is the Gamma function, and $\overline{E(r)}$ is the mean broadband energy at a given range r from the source. The theoretical Gamma distribution of Eq. (8) is plotted over each histogram in Figs. 8–10 using the calibrated results for mean energy $\overline{E(r)}$ from Sec. III B and μ from Sec. II D. For the bandpassed center frequency data, the theoretical exponential distribution is a special case of the Gamma distribution where $\mu = 1$. For each case, the theoretical statistical distributions, $P(E(r))$, at six different ranges are each calculated using the range value centered within the range window used for each histogram. The distributions change as the ex-

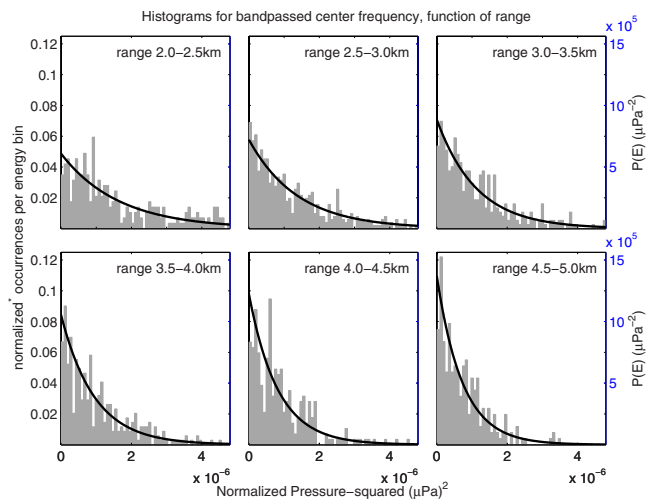


FIG. 8. (Color online) Histograms of the received center frequency energies are separated by range in 500 m increments and plotted against the calibrated model energy distribution. The histograms are normalized by dividing the number of occurrences in each energy bin with the total number of energy measurements at the specified range. The right axis for the theoretical distribution is scaled to provide direct visual comparison of the theoretical distribution with the histogram.

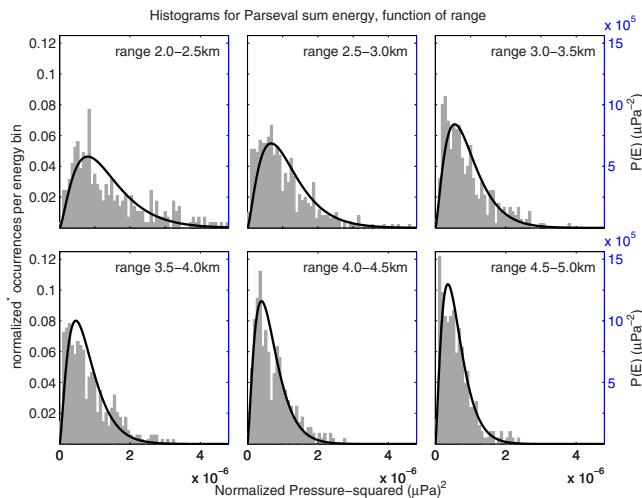


FIG. 9. (Color online) Histograms of the received broadband PS energies, plotted similar to Fig. 5.

pected broadband energy $\overline{E(r)}$ decreases with range. For all three measurements, the histograms closely match the theoretical distributions.

The statistical distributions for the data here are similar to those found in Ref. 9 for the same area. In that experiment, broadband 100 Hz bandwidth signals centered at 400 Hz were transmitted along two different propagation paths of 42 and 60 km. The intensities were found to scintillate according to similar types of distributions. At those ranges, the peak MF energy level in decibels approximated a log-normal distribution, which is a special case of the distribution expressed in Eq. (8) for a large time-bandwidth product. The distribution of the point intensity closely followed an exponential distribution, approximating an instantaneous measurement of a statistically saturated acoustic field. Here, the distributions are plotted on a linear scale and the histograms are grouped over range intervals to show how the distributions vary as a function of range. Also, the distributions here use data collected at different locations in space and are therefore functions of scintillation over both time and space.

F. Matched filter degradation

The 20-ping averaged MF degradation in decibels, given by the difference between the mean PS and MF levels, can be estimated from Fig. 6(a) for the 390–440 Hz data. In addition to modal dispersion, this difference may also be caused by ambient noise or reverberation integrated into the PS measurement. These effects are negligible for our signals within the analysis time T . The MF degradation for the individual transmitted signals plotted in Fig. 11(a) shows significant fluctuation. The 20-ping averaged mean degradation in Fig. 11(b) illustrates an approximate linear increase with range. The range-dependent MF degradation D_{MF} can be approximated using the calibrated results from Sec. III B through the linear relationship

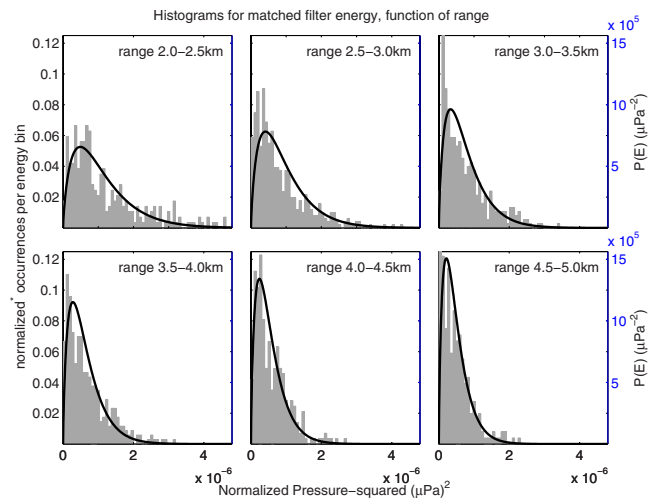


FIG. 10. (Color online) Histograms of the received broadband MF energies, plotted similar to Fig. 5.

$$D_{MF}(\rho) = c + m\rho, \quad (9)$$

where c is an initial offset at the onset of modes and $m\rho$ accounts for cumulative dispersion in the waveguide. For these 390–440 Hz data, $c=0.7$ dB and $m=0.05$ dB/km, as shown in Table II. The latter linear decibel increase in degradation with range corresponds to an exponential decay of the MF energy with range when compared to the PS energy. The mean MF degradation in Fig. 11 is biased slightly above the calibrated MF degradation because the mean is taken over log values resulting in a bias that depends on the variance of the MF degradation.

G. Monte Carlo simulations for broadband acoustic transmissions through a random waveguide for field statistics

In this section, Monte Carlo simulations are used to simulate sound speed fluctuations in a random waveguide and propagate the broadband acoustic signals through the waveguide. We show that the statistics of simulated acoustic transmissions through the dynamic environment are consistent with the observed statistics of the data in Sec. II D.

Internal waves randomize the ocean by causing fluctuations in water-column temperature and sound speed profiles over both space and time by adiabatic vertical displacements. This phenomenon has been shown to be the primary source for acoustic field randomization in continental shelf environments.^{4,6,35,37,40–42} More recent work has furthered the understanding of intensity fluctuations caused by both linear diffuse internal waves,⁴³ which create a gradual continuous fluctuation in the sound speed structure, and nonlinear internal waves^{4–7} or solitons, which create more discontinuous sound speed fluctuations in range. Both the 1995 SWARM and the 1996 PRIMER experiments, conducted on the New Jersey shelf, found that linear internal waves cause broadband intensity scintillation while nonlinear solitons further randomize and attenuate the intensity through mode coupling and mode stripping.^{4–7}

Creating an accurate model for both the linear diffuse internal waves and the nonlinear solitons is challenging with-

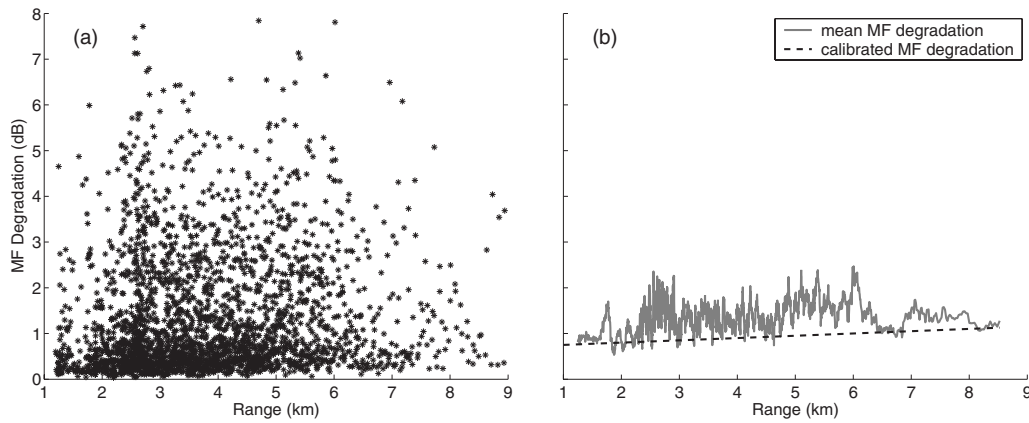


FIG. 11. The MF degradation in the 390–440 Hz data is illustrated here for (a) each received signal and (b) using a running average over 20 transmissions. The average is compared to the calibrated degradation.

out highly detailed environmental data such as real-time sound speed and temperature profiles measured continuously in time and space. The SWARM and PRIMER experiments observed both linear and nonlinear internal waves in the same region as this experiment. Both were conducted in July and August when the internal wave activity is the strongest and most prevalent⁵ while the MAE was conducted in April–May when the intensity and prevalence of internal waves are weaker. The experimentally measured sound speed profiles from the New Jersey continental shelf during April–May 2003 shown in Fig. 2 provide a good sample of the profiles measured at different locations and times on the continental shelf; however, they are too aliased to observe specific internal waves.

Given these limitations, a simpler approach is taken for modeling the environment. We assume the statistics of the sound speed profiles are stationary over the region of the experiment. Linear internal waves are simulated by updating the sound speed profiles in range every 500 m, chosen as an approximate correlation length observed for continental shelf environments.^{4,37} The profiles are selected randomly from the experimentally collected sound speed profiles. This approach is taken because it is impossible to predict the direction, amplitude, and frequency of specific internal waves. Instead, a sufficient sample of the observed sound speed profiles are used to simulate the *effects* of the internal waves after many independent simulations. Discontinuous solitons

are not included in the model because their presence cannot be confirmed between the source and the receiver for any given transmission. The linear diffuse internal waves are largely responsible for the scintillation in the broadband intensity interference pattern and are therefore sufficient for the first order statistics such as the mean and standard deviations of the intensities. This model does not describe the temporal coherence of the scintillating acoustic field or intensity because the model relies only on independent realizations of the environment. The temporal coherence of the acoustic intensity could be calculated if the temporal fluctuations of the environment caused by internal waves were included into the model.

The acoustic field through this fluctuating environment is modeled using the RAM,³² which takes into account the environmental parameters including sea-bottom geoacoustic properties, source and receiver locations, varying bathymetry between source and receiver, and the dynamic sound speed profile. For each realization, it produces the time-harmonic Green’s function $G(\mathbf{r}|\mathbf{r}_0, f)$ in space at frequency f from which we can determine the complex spectral amplitude,

$$\Phi_m(\mathbf{r}|\mathbf{r}_o, f) = Q(f)G(\mathbf{r}|\mathbf{r}_o, f), \quad (10)$$

where the subscript m indicates that it is a modeled output. Here, $Q(f)$ is the Fourier transform for a synthesized source signal. Applying the RAM over the source bandwidth fol-

TABLE II. The results of calibration for source level correction c_{SL} and TL decay rate correction, α , are shown here for both PS and MF energy over three frequency bands. The MF degradation is found as the difference of the PS value and MF value for both source level and range-dependent degradation. For the two higher frequency bands, there were fewer transmissions occurring over a smaller window in range for which to calibrate the expected levels. This results in higher error bounds for the estimates of c_{SL} and α . For the highest frequency band, the transmission data across the array for each transmission are highly correlated, so the error bounds calculated for the 875–975 Hz band are used as an upper limit for the error bounds.

	390–440 Hz		875–975 Hz		1200–1400 Hz	
	c_{SL} (dB)	α (dB/km)	c_{SL} (dB)	α (dB/km)	c_{SL} (dB)	α (dB/km)
Parseval sum	-0.8 ± 0.2	-0.03 ± 0.04	-1.1 ± 0.6	-0.09 ± 0.20	0.8 ± 0.6	-0.06 ± 0.20
Matched filter	-1.5 ± 0.2	-0.08 ± 0.04	-1.7 ± 0.8	-0.26 ± 0.20	-0.8 ± 0.8	-0.08 ± 0.20
MF degradation	0.7	0.05	0.6	0.17	1.6	0.02

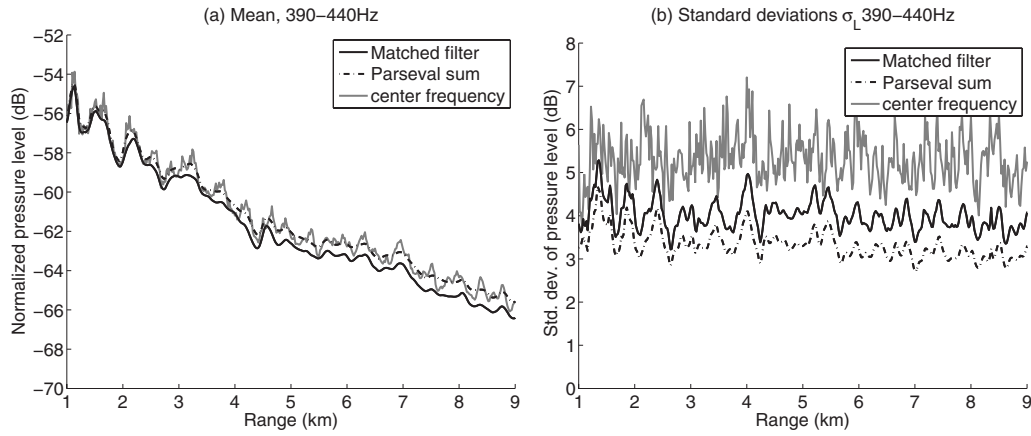


FIG. 12. The (a) mean and (b) standard deviations for the 390–440 Hz MF, PS, and center frequency energies modeled using Monte Carlo simulations in a waveguide randomized by internal waves. The statistics of the model match those of the data in Fig. 6.

lowing Eqs. (2) and (4) provides the modeled PS, $E_{PS,m}$ and MF energies, $E_{MF,m}$. For example the modeled PS energy is expressed as

$$E_{PS,m}(\mathbf{r}|\mathbf{r}_0) = \int_{f_i}^{f_f} |\Phi_m(\mathbf{r}|\mathbf{r}_0, f)|^2 df, \quad (11)$$

and the modeled mean broadband PS transmission loss is $10 \log_{10}$ of the received mean PS energy, averaged over all realizations, normalized by the source energy E_0 ,

$$\begin{aligned} TL_m(\mathbf{r}|\mathbf{r}_0) &= 10 \log_{10} \left(\frac{1}{E_0} \langle E_{PS,m}(\mathbf{r}|\mathbf{r}_0) \rangle \right) \\ &= 10 \log_{10} \left(\frac{1}{E_0} \left\langle \int_{f_i}^{f_f} |Q(f)|^2 |G(\mathbf{r}|\mathbf{r}_0, f)|^2 df \right\rangle \right), \end{aligned} \quad (12)$$

where $E_0 = \int_{f_i}^{f_f} |Q(f)|^2 df$.

To illustrate the modeled field statistics, we implement this Monte Carlo model for a dynamic waveguide with a constant water depth of 85 m and a sand bottom halfspace. Figure 12 illustrates the means and standard deviations for 100 realizations of the MF, PS, and center frequency energies using a normalized 0 dB re 1 μ Pa source level for the 390–440 Hz band. Each of the 100 realizations of the broadband energy were computed with a spectral spacing of 1 Hz over the 50 Hz bandwidth, leading to a total of 5000 time-harmonic runs to generate the expected PS and MF energies.

The statistics derived from the model closely match those of the data in Fig. 6. For instance, the model PS energy standard deviation is the smallest, while that for the center frequency is the largest, consistent with the data. This implies that this approach can be applied to reliably model the acoustic field statistics on the New Jersey continental shelf.

III. COMPUTATIONALLY EFFICIENT NUMERICAL APPROACH FOR ESTIMATING MEAN BROADBAND TRANSMISSION LOSS IN A FLUCTUATING RANGE-DEPENDENT OCEAN WAVEGUIDE

In wide area sonar applications, the mean TL must be efficiently estimated in order to detrend sonar imagery and invert for scattering strength or target strength of scatterers

and source level of radiating targets over vast areas.^{2,14} The brute-force method described in Sec. II G for estimating the expected broadband TL is far too computationally intensive and impractical for realistic sonar operations. Wide area sonar can image circular areas with a diameter exceeding 100 km. Imaged objects include fish shoals that often occupy areas spanning more than $20 \times 20 \text{ km}^2$.² In order to invert for areal scattering strengths in these images, the bistatic TL both from the source and to the receiver must be estimated over the entire area and updated for each image with a moving receiver. For example, a large fish shoal extending 20 km in cross range may span 60° at 20 km range from the source, requiring 60 TL transects to be estimated at 1° spacing (roughly equal to the broadside angular resolution of a wide area sonar system).^{2,14} For each transect requiring 5000 time harmonic simulations, a total of 300 000 runs are required to estimate the mean broadband TL and subsequently the areal scattering strengths throughout the shoal.

Here we propose a numerically efficient approach for estimating the expected broadband energy and mean TL through a fluctuating range-dependent ocean waveguide. We show that the mean broadband energy can be estimated to within a 0.5 dB standard deviation using three Monte Carlo simulations at only the center frequency and by introducing range and depth averaging for each radial. This significantly reduces the number of time-harmonic Monte Carlo runs from 300 000 to just 180 for the 60° span of the sonar imagery described above. These 180 runs can be computed within minutes to allow near real-time inversion of wide-area sonar imagery for fish areal scattering strengths and population density estimates.²

A. Approximating mean broadband transmission loss

We illustrate the computationally efficient approach for estimating the mean broadband TL in a fluctuating ocean waveguide for two different waveguides with sandy bottoms in Figs. 13(a) and 13(b). The first has a constant water depth of 85 m and the second has an upslope bathymetry, as shown in Fig. 13(d). For comparison, the 100 Monte Carlo realiza-

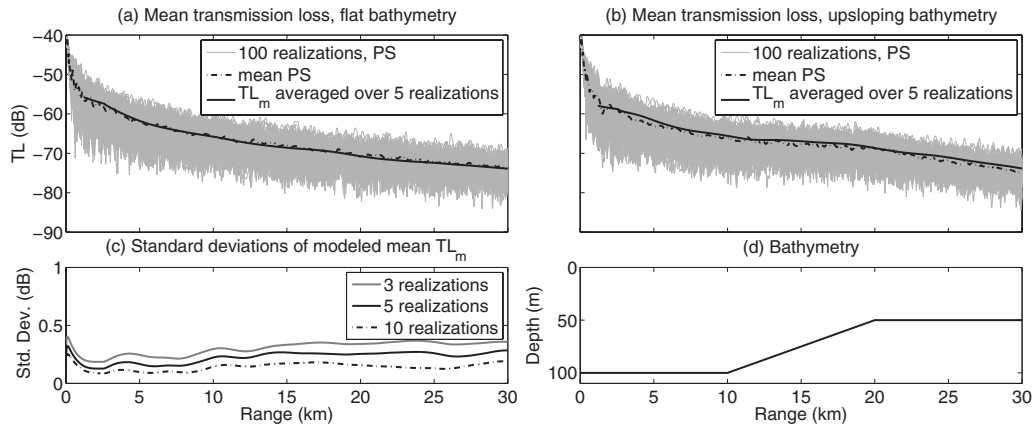


FIG. 13. The mean broadband PS TL over 100 realizations of the Monte Carlo model are compared to the approximate model that uses the center frequency TL found by averaging over the first five realizations and using a spatial average over both range and depth. The results are illustrated for environments with (a) constant and (b) upsloping bathymetry where the bathymetry is plotted in (d). In (c) the standard deviations for this modeled mean TL are shown as a function of range averaging over 3, 5, and 10 Monte Carlo realizations.

tions of the full broadband PS TL are plotted along with the ensemble average over these 100 realizations for both waveguides.

We next approximate the mean broadband TL as

$$\begin{aligned} \text{TL}_{m,N}(\mathbf{r}|\mathbf{r}_0) &\approx 10 \log_{10}(I_{m,N}(\mathbf{r}|\mathbf{r}_0, f_c)) \\ &= 10 \log_{10} \left\{ \frac{1}{N} \sum_{p=1}^N \overline{|G_p(\mathbf{r}|\mathbf{r}_0, f_c)|^2} \right\}, \end{aligned} \quad (13)$$

which is obtained by averaging over N , only a few independent realizations of the acoustic field at the center frequency with the overline indicating spatial averaging of the Green's function magnitude square over both depth and range. Here, the magnitude squared Green's function output of the RAM is averaged about the receiver over ± 20 m in depth and in range using a range dependent Hanning window with an extent given by $1.5 \log(r/(1 \text{ km}))$ km. We first average the model over $N=5$ independent realizations to reduce the standard deviation of the approximate mean TL to less than 0.5 dB. At ranges greater than 2 km, this approximate $\text{TL}_{m,5}$ follows a monotonic decay and matches the averaged broadband PS TL from 100 Monte Carlo realizations (with 5000 time-harmonic runs) to within 0.5 dB, as shown in Figs. 13(a) and 13(b).

Figure 13(c) illustrates how averaging over different numbers of independent Monte Carlo realizations for the environment with constant bathymetry reduces the standard deviation of the approximate TL model. In this case, the standard deviation is still less than 0.5 dB out to 30 km range even when using only $N=3$ realizations.

The spatial window used for depth and range averaging is chosen to be large enough to subtend at least one modal cycle, but not too large as to average out the attenuation in range or the effects caused by channeling of the acoustic energy in the water column. This spatial averaging bears some resemblance to the range averaging used by Harrison and Harrison,⁴⁴ where range averaging is used to replace a frequency averaging over the bandwidth in a *deterministic* environment. Here, both range and depth averaging are applied in order to estimate the *mean* transmission loss in a

random environment. Averaging the intensity over depth has a similar effect as averaging over independent realizations of the environment; both reduce the variance caused by modal interference in a waveguide randomized by internal waves.

B. Calibration of broadband expected intensity model

Here, we calibrate the computationally efficient model for mean broadband TL with data from the New Jersey Strataform. The PS energy level differs from the TL by the source level, $L_{\text{PS}} = \text{SL} + \text{TL}$. A maximum likelihood estimator (MLE) is employed to correct the modeled expected broadband intensity for any inaccuracies in source level and the waveguide attenuation decay rate.

In long range sonar applications, the source level is determined by the coherent interaction of multiple source elements in the far field of the array. While the individual transducer elements have been calibrated by the manufacturer in tanks, the resultant output source power still needs to be calibrated in the field since it is dependent on the number of elements operating at any given time and the input power applied to each element.

The mean TL decay trend, discussed in Sec. III A, depends not only on geometrical spreading loss and absorption into the seafloor, but also on absorption and scattering losses of the ocean environment from bubble clouds, nonlinear solitons, fish, and other scatterers in the water column. These parameters may not be completely characterized in the propagation model. We introduce an attenuation correction coefficient a to the model to account for incomplete knowledge of all absorption and scattering loss mechanisms in the environment,

$$\overline{E_m(\mathbf{r}|\mathbf{r}_0)} \approx E_0 I_{m,N}(\mathbf{r}|\mathbf{r}_0, f_c) \exp(2a|\boldsymbol{\rho} - \boldsymbol{\rho}_0|), \quad (14)$$

where $|\boldsymbol{\rho} - \boldsymbol{\rho}_0|$ is the horizontal separation between the source and the receiver. Equation (14) is a good approximation for waveguides at ranges where the field is dominated by low order modes that propagate at elevation angles close to the horizontal where the attenuation is approximately constant over the modes.

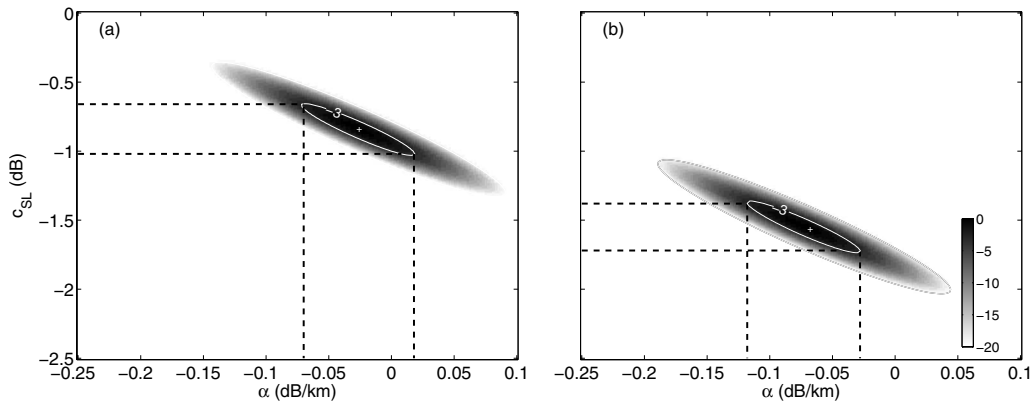


FIG. 14. The normalized log-likelihood function shown here for both (a) PS and (b) MF energy levels to calibrate for both source level and the range-dependent attenuation correction.

This model is applied to estimate the expected intensity level over range for the MAE. A MLE estimates parameters a and E_0 by comparing the broadband data from Sec. II D with the modeled mean intensity of Eq. (14). These parameters can then be applied, respectively, as corrections to the mean TL decay with range $\alpha|\rho - \rho_0|$, where $\alpha = 20 \log_{10}(e)a$, and correction to the source level, $c_{SL} = 10 \log_{10}(E_0/E_{0(\text{uncorrected})})$, where $E_{0(\text{uncorrected})}$ is an uncalibrated nominal value for source energy which may be obtained, for instance, from the transducer manufacturer's specification. Note that a calibration relying entirely on data that does not employ an acoustic propagation model would fail to take into account first order changes in the TL such as focusing effects caused by bathymetric variations along different transects in range-dependent environments, as well as changes in mean water-column sound speed and bottom geoacoustic parameters.

We assume that the received broadband signal from each transmission is statistically independent. The joint probability density function for the N received energy measurements from Eq. (8) is

$$p(E(r_1), E(r_2), \dots, E(r_N)) = \prod_{i=1}^N \frac{(\mu/\overline{E(r_i)})^\mu E(r_i)^{\mu-1} \exp(-\mu E(r_i)/\overline{E(r_i)})}{\Gamma(\mu)}, \quad (15)$$

where $E(r_i)$ is the broadband intensity measured for the i th

received signal with source-receiver separation r_i . The corresponding expected intensity $\overline{E(r_i)}$ is obtained from Eq. (14) incorporating the modeled expected TL for each transmission with source-receiver separation of r_i . Taking $10 \log_{10}$ of Eq. (15) we obtain the log-likelihood function for the data. Equation (15) allows for a method to correct for unknown parameters in the model, in this case E_0 and a . The log-likelihood function depends nonlinearly on these two parameters, making it challenging to obtain a MLE for these parameters analytically. Here, the log-likelihood function is plotted onto a two dimensional ambiguity surface for E_0 and a , where the maximum value indicates the most probable value for the correction to source level and range-dependent correction to transmission loss.

The log-likelihood function is plotted for the model calibration with the 390–440 Hz PS energy data in Fig. 14(a), normalized by its maximum value. The contour line marks the -3 dB value, which indicates where the statistical likelihood is half that at the maximum. The correction to source level is found to be -0.8 dB for PS, estimated within an error bound of ± 0.2 dB, and the attenuation correction α is found to be -0.03 dB/km within an error bound of ± 0.04 dB/km as tabulated in Table II. The matched filtered energy data may also be calibrated using the same approach. The corresponding normalized ambiguity surface is plotted in Fig. 14(b) and the results tabulated are in Table II. The difference

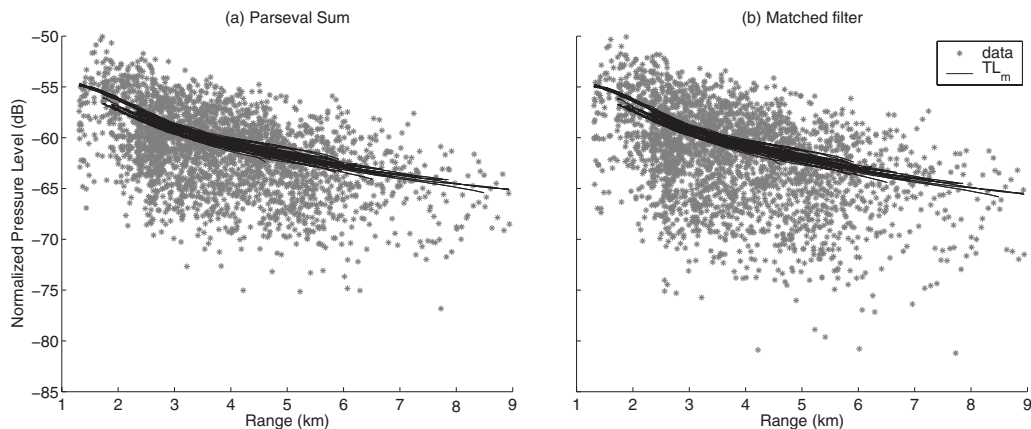


FIG. 15. The normalized expected energy level plotted over the broadband data in frequency range 390–440 Hz, measured with a single desensitized hydrophone, for the (a) PS and (b) MF.

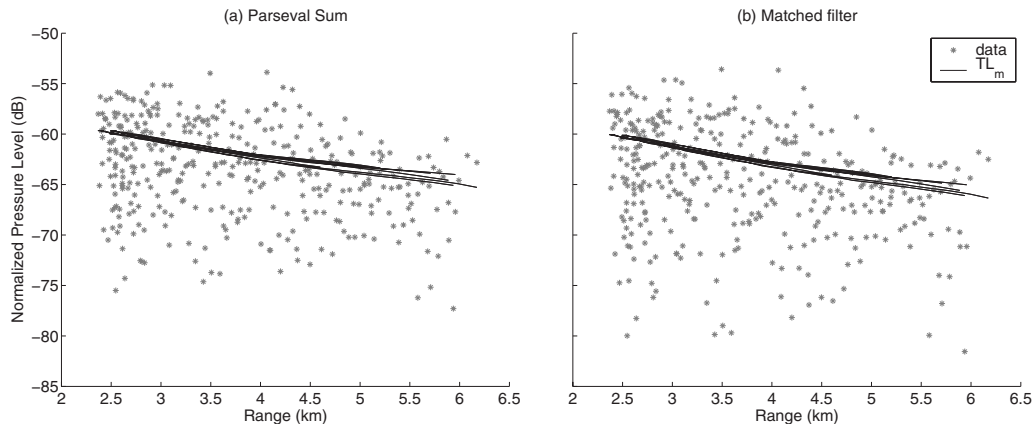


FIG. 16. The normalized expected energy level plotted over the broadband data in frequency range 875–975 Hz, measured with a single desensitized hydrophone, for the (a) PS and (b) MF.

in calibration for the PS and MF data provides a measure of the MF degradation where $c = 10 \log_{10}(E_{0,PS}/E_{0,MF}) \approx 0.7$ dB and $m = 4.34(a_{PS} - a_{MF}) \approx 0.05$ dB/km.

The normalized expected pressure level from the calibrated model is plotted along with the 390–440 Hz data for both PS and MF in Figs. 15(a) and 15(b), respectively. The modeled mean level is plotted for each track of the experiment and follows the trend of the data closely at all ranges. Differences in the modeled mean levels for the different tracks occur because the modeled TL takes into account bathymetric variations, and source and receiver depth changes. The calibration results for the higher frequency bands, 875–975 Hz and 1250–1400 Hz, are provided in Table II and plotted in Figs. 16 and 17, respectively.

The proposed approach for calibrating the source level from the measured data makes a number of assumptions. (1) The source level is stationary over the time period of the experiment, and has a variance that is small compared to the variance caused by fluctuations in the environment. (2) The environmental fluctuation is assumed to follow a stationary process over both space and time of the experiment. (3) The initial assumption in Eq. (14) that the TL correction takes on the form $\exp(2a|\rho - \rho_0|)$ may be inaccurate when large attenuation corrections are required. It assumes that the correction in range affects each mode equally. This would not be

the case if there is significant energy propagating in the higher order modes or if there is significant mode coupling and mode stripping. For the current data set, the received signal energy is mostly contained in lower order modes beyond 2 km, as discussed in Sec. II C. (4) The corrections to the mean TL should only be applied at propagation distances within the source-receiver ranges where the data were analyzed. For instance, a TL correction of -0.08 dB/km for the MF signal energy should not be extrapolated for ranges too far beyond 10 km range where the data were present.

IV. CONCLUSION

The scintillation statistics of broadband acoustic transmissions in a continental shelf waveguide have been quantified as a function of signal bandwidth B , center frequency f_c , and range. The received signal energy is shown to follow the Gamma distribution implying the instantaneous field is fully saturated from multimodal propagation contributions following the central limit theorem. The Gamma distribution depends on the mean energy, determined as a function of source-receiver separation, and the number of independent statistical fluctuations or coherent cells μ of the received signal determined from the energy standard deviations. The number of coherent cells μ is calculated for several standard

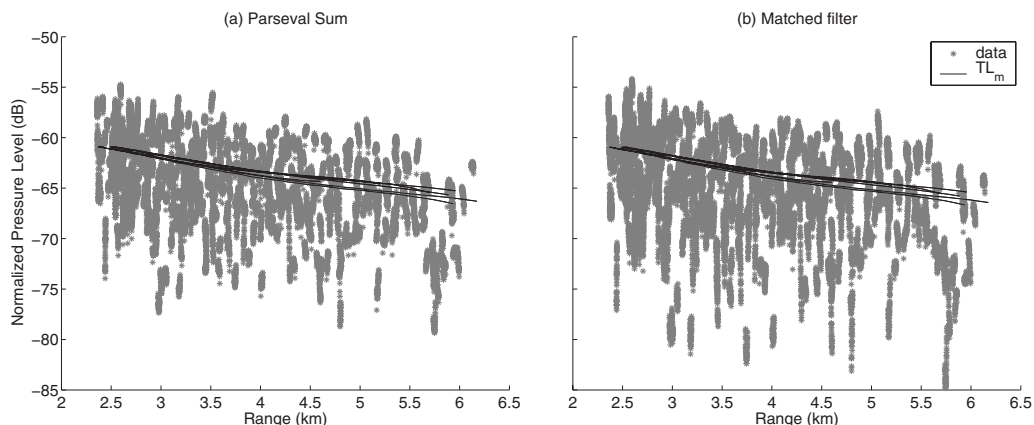


FIG. 17. The normalized expected energy level plotted over the broadband data in frequency range 1250–1400 Hz, measured with an array of 64 hydrophones for the (a) PS and (b) MF.

receivers in ocean acoustics, such as the MF, the PS and the bandpass center frequency. It is found that μ of the received signal is an order of magnitude smaller than the time-bandwidth product TB of the transmitted signal. An empirical relationship is derived showing the monotonically increasing dependence of μ on the relative bandwidth B/fc .

A computationally efficient numerical approach is presented for rapidly estimating the range-dependent mean broadband TL over wide areas of an ocean waveguide. The mean TL is estimated from Monte Carlo simulations using a range-dependent propagation model with only three to five realizations of the acoustic field in an ocean waveguide with random sound speed fluctuations. The approach uses incoherent spatial averaging over both range and depth for the time-harmonic intensity at the center frequency to estimate the mean broadband TL for a statistically saturated environment. A MLE applied to the data is used to calibrate the model for source level and the mean TL decay rate over range. This approach is indispensable for inverting wide-area sonar imagery for scattering properties of distributed targets.

ACKNOWLEDGMENTS

The authors would like express our appreciation toward Nicholas Makris for insightful discussion and clarification on the topic. This research was conducted with funding support from the Office of Naval Research Ocean Acoustics Program, the National Oceanographic Partnership Program, and the Alfred P. Sloan Foundation. This research is a contribution to the Census of Marine Life. The authors would also like to thank Northeastern University's Bernard M. Gordon Center for Subsurface Sensing and Imaging Systems for administrative support.

¹W. Burdick, *Underwater Acoustic System Analysis*, 2nd ed. (Prentice-Hall, Englewood, NJ, 1990).

²N. C. Makris, P. Ratilal, D. T. Symonds, S. Jagannathan, S. Lee, and R. W. Nero, "Fish population and behavior revealed by instantaneous continental shelf-scale imaging," *Science* **311**, 660–663 (2006).

³T. Yang and W.-B. Yang, "Performance analysis of direct-sequence spread-spectrum underwater acoustic communications with low signal-to-noise-ratio input signals," *J. Acoust. Soc. Am.* **123**, 842–855 (2000).

⁴R. Headrick, J. F. Lynch, J. Kemp, A. Newhall, K. von der Heydt, J. R. Apel, M. Badiy, C.-S. Chiu, S. Finette, M. H. Orr, B. H. Pasewark, A. Turgut, S. Wolf, and D. Tielburger, "Acoustic normal-mode fluctuation statistics in the 1995 swarm internal wave scattering experiment," *J. Acoust. Soc. Am.* **107**, 201–220 (2000).

⁵J. R. Apel, L. A. Ostrovsky, Y. A. Stepanyants, and J. F. Lynch, "Internal solitons in the ocean and their effect on underwater sound," *J. Acoust. Soc. Am.* **121**, 695–722 (2007).

⁶D. Tielburger, S. Finette, and S. Wolf, "Acoustic propagation through an internal wave field in a shallow water waveguide," *J. Acoust. Soc. Am.* **101**, 789–807 (1997).

⁷J. Preisig and T. Duda, "Coupled acoustic mode propagation through continental-shelf internal solitary waves," *IEEE J. Ocean. Eng.* **22**, 256–269 (1997).

⁸S. Ramp, C. Chiu, F. Bahr, Y. Qi, P. Dahl, J. Miller, J. Lynch, R. Zhang, and J. Zhou, "The shelf-edge frontal structure in the central east China sea and its impact on low frequency acoustic propagation," *IEEE J. Ocean. Eng.* **29**, 1011–1031 (2004).

⁹A. Fredericks, J. A. Colosi, J. Lynch, C. Chiu, and P. Abbot, "Analysis of multipath scintillation from long range acoustic transmissions on the New England continental slope and shelf," *J. Acoust. Soc. Am.* **117**, 1038–1057 (2005).

¹⁰P. Worcester, G. Williams, and S. Flatté, "Fluctuations of resolved acoustic multipaths at short range in the ocean," *J. Acoust. Soc. Am.* **70**, 825–840

(1981).

¹¹F. J. Beron-Vera, M. G. Brown, J. A. Colosi, S. Tomovic, A. L. Virovlyansky, M. A. Wolfson, and G. M. Zaslavsky, "Ray dynamics in long range acoustic propagation experiment," *J. Acoust. Soc. Am.* **114**, 1226–1242 (2003).

¹²R. Urlick, *Principles of Underwater Sound* (McGraw-Hill, New York, 1983).

¹³S. Kay, *Fundamentals of Statistical Signal Processing, Detection Theory* Vol. 2 (PTR Prentice-Hall, Englewood, NJ, 1998).

¹⁴A. Galinde, N. Donabed, M. Andrews, S. Lee, N. C. Makris, and P. Ratilal, "Range-dependent waveguide scattering model calibrated for bottom reverberation in a continental shelf environment," *J. Acoust. Soc. Am.* **123**, 1270–1281 (2008).

¹⁵N. C. Makris, "The effect of saturated transmission scintillation on ocean acoustic intensity measurements," *J. Acoust. Soc. Am.* **100**, 769–783 (1996).

¹⁶J. W. Goodman, *Statistical Optics* (Wiley, New York, 1985).

¹⁷S. O. Rice, "A statistical analysis of random noise," *Bell Syst. Tech. J.* **24**, 46–108 (1945).

¹⁸N. C. Makris, "Parameter resolution bounds that depend on sample size," *J. Acoust. Soc. Am.* **99**, 2851–2861 (1996).

¹⁹G. L. Turin, "An introduction to matched filters," *IRE Trans. Inf. Theory* **IT-6**, 311–329 (1960).

²⁰P. Ratilal, Y. Lai, D. T. Symonds, L. A. Ruhlmann, J. R. Preston, E. K. Scheer, M. T. Garr, C. W. Holland, J. A. Goff, and N. C. Makris, "Long range acoustic imaging of the continental shelf environment: The acoustic clutter reconnaissance experiment 2001," *J. Acoust. Soc. Am.* **117**, 1977–1998 (2005).

²¹D. Rouseff, "Intersymbol interference in underwater acoustic communications using time-reversal signal processing," *J. Acoust. Soc. Am.* **117**, 780–788 (2005).

²²R. Barr, "A design study of an acoustic system suitable for differentiating between orange roughy and other New Zealand deep-water," *J. Acoust. Soc. Am.* **109**, 164–178 (2001).

²³E. McDaid and G. Gaunard, "Signal processing of ideal echoes resonantly scattered by underwater structures," *J. Acoust. Soc. Am.* **88**, 2720–2735 (1990).

²⁴D. Chu and T. Stanton, "Application of pulse compression techniques to broadband acoustic scattering by live individual zooplankton," *J. Acoust. Soc. Am.* **104**, 39–55 (1998).

²⁵Y. Lai, "Acoustic scattering from stationary and moving targets in shallow water environments: With application of humpback whale detection and localization," Ph.D. thesis, MIT, Cambridge, MA, 2004).

²⁶N. Levanon, *Radar Principles* (Wiley, New York, 1988).

²⁷G. Bar-Yehoshua, "Quantifying the effect of dispersion in continental shelf sound propagation," MS thesis, MIT, Cambridge, MA, 2002).

²⁸Y. H. Goh, P. Gerstoft, W. Hodgkiss, Jr., and C.-F. Huang, "Statistical estimation of transmission loss from geoacoustic inversion using a towed array," *J. Acoust. Soc. Am.* **122**, 2871–2579 (2007).

²⁹D. Tollefsen, S. Dosso, and M. Wilmut, "Matched-field geoacoustic inversion with a horizontal array and low-level source," *J. Acoust. Soc. Am.* **120**, 221–230 (2006).

³⁰L. Sha and L. Nolte, "Effects of environmental uncertainties on sonar detection performance prediction," *J. Acoust. Soc. Am.* **117**, 1942–1953 (2005).

³¹N. C. Makris, L. Z. Avelino, and R. Menis, "Deterministic reverberation from ocean ridges," *J. Acoust. Soc. Am.* **97**, 3547–3574 (1995).

³²M. D. Collins, "Generalization of the split-step pade," *J. Acoust. Soc. Am.* **96**, 382–385 (1994).

³³J. A. Goff, D. J. P. Swift, C. S. Duncan, L. A. Mayer, and J. Hughes-Clark, "High resolution swath sonar investigation of sand ridge, dune and ribbon morphology in the offshore environment of the New Jersey margin," *Mar. Geol.* **161**, 307–337 (1999).

³⁴J. Goff, B. J. Kraft, L. A. Mayer, S. G. Schock, C. K. Sommerfield, H. C. Olson, S. P. S. Golick, and S. Nordfjord, "Seabed characterization on the new jersey middle and outer shelf: Correlatability and spatial variability of seafloor sediment properties," *Mar. Geol.* **209**, 147–172 (2004).

³⁵P. Ratilal and N. C. Makris, "Mean and covariance of the forward field propagated through a stratified ocean waveguide with three-dimensional random inhomogeneities," *J. Acoust. Soc. Am.* **118**, 3532–3559 (2005).

³⁶M. B. Porter and E. L. Reiss, "A numerical method for ocean acoustic normal modes," *J. Acoust. Soc. Am.* **76**, 244–252 (1984).

³⁷J. R. Apel, M. Badiy, C.-S. Chiu, S. Finette, R. Headrick, J. Kemp, J. F. Lynch, A. Newhall, M. H. Orr, B. H. Pasewark, D. Tielburger, A. Turgut,

- K. von der Heydt, and S. Wolf, "An overview of the 1995 swarm shallow-water internal wave acoustic scattering experiment," *IEEE J. Ocean. Eng.* **22**, 465–500 (1997).
- ³⁸S. Finette, M. H. Orr, A. Turgut, J. R. Apel, M. Badiéy, C.-S. Chiu, R. Headrick, J. Kemp, J. F. Lynch, A. Newhall, K. von der Heydt, B. H. Pasewark, S. N. Wolf, and D. Tielbuerger, "Acoustic field variability induced by time evolving internal wave fields," *J. Acoust. Soc. Am.* **108**, 957–972 (2000).
- ³⁹D. Rouseff, A. Turgut, S. Wolf, S. Finette, M. Orr, B. Pasewark, J. Apel, M. Badiéy, C.-S. Chiu, R. Headrick, J. Lynch, J. Kemp, A. Newhall, and D. Tielbuerger, "Coherence of acoustic modes propagating through shallow water internal waves," *J. Acoust. Soc. Am.* **111**, 1655–1666 (2002).
- ⁴⁰J. Lynch, G. Jin, R. Pawlowicz, D. Ray, A. Plueddeman, C. Chiu, J. Miller, R. Bourke, A. Parsons, and R. Muench, "Acoustic travel-time perturbations due to shallow-water internal waves and internal tides in the Barents sea polar front: Theory and experiment," *J. Acoust. Soc. Am.* **99**, 803–821 (1996).
- ⁴¹T. Duda and J. Presig, "A modeling study of acoustic propagation through moving shallow water solitary wave packets," *IEEE J. Ocean. Eng.* **24**, 16–32 (1999).
- ⁴²T. Chen, P. Ratilal, and N. C. Makris, "Mean and variance of the forward field propagated through three-dimensional random internal waves in a continental-shelf waveguide," *J. Acoust. Soc. Am.* **118**, 3560–3574 (2005).
- ⁴³D. Creamer, "Scintillating shallow water waveguides," *J. Acoust. Soc. Am.* **99**, 2825–2838 (1996).
- ⁴⁴C. H. Harrison and J. A. Harrison, "A simple relationship between frequency and range averages for broadband sonar," *J. Acoust. Soc. Am.* **97**, 1314–1317 (1995).